



# Optical measurement of microvascular oxygenation and blood flow responses in awake mouse cortex during functional activation

Journal of Cerebral Blood Flow & Metabolism  
2022, Vol. 42(3) 510–525  
© The Author(s) 2020  
Article reuse guidelines:  
sagepub.com/journals-permissions  
DOI: 10.1177/0271678X20928011  
journals.sagepub.com/home/jcbfm



İkbal Şencan<sup>1</sup> , Tatiana Esipova<sup>2,3</sup>, Kivılcım Kılıç<sup>4</sup>,  
Baoqiang Li<sup>1</sup>, Michèle Desjardins<sup>5</sup>, Mohammad A Yaseen<sup>1</sup>,  
Hui Wang<sup>1</sup>, Jason E Porter<sup>1</sup>, Sreekanth Kura<sup>4</sup>, Buyin Fu<sup>1</sup>,  
Timothy W Secomb<sup>6</sup> , David A Boas<sup>4</sup>, Sergei A Vinogradov<sup>2,3</sup>,  
Anna Devor<sup>1,4,7,8</sup> and Sava Sakadžić<sup>1</sup>

## Abstract

The cerebral cortex has a number of conserved morphological and functional characteristics across brain regions and species. Among them, the laminar differences in microvascular density and mitochondrial cytochrome c oxidase staining suggest potential laminar variability in the baseline O<sub>2</sub> metabolism and/or laminar variability in both O<sub>2</sub> demand and hemodynamic response. Here, we investigate the laminar profile of stimulus-induced intravascular partial pressure of O<sub>2</sub> (pO<sub>2</sub>) transients to stimulus-induced neuronal activation in fully awake mice using two-photon phosphorescence lifetime microscopy. Our results demonstrate that stimulus-induced changes in intravascular pO<sub>2</sub> are conserved across cortical layers I–IV, suggesting a tightly controlled neurovascular response to provide adequate O<sub>2</sub> supply across cortical depth. In addition, we observed a larger change in venular O<sub>2</sub> saturation ( $\Delta sO_2$ ) compared to arterioles, a gradual increase in venular  $\Delta sO_2$  response towards the cortical surface, and absence of the intravascular “initial dip” previously reported under anesthesia. This study paves the way for quantification of layer-specific cerebral O<sub>2</sub> metabolic responses, facilitating investigation of brain energetics in health and disease and informed interpretation of laminar blood oxygen level dependent functional magnetic resonance imaging signals.

## Keywords

Intravascular partial pressure of oxygen, cortical layers, neurovascular coupling, oxygen extraction fraction, two-photon microscopy

Received 24 November 2019; Revised 9 April 2020; Accepted 14 April 2020

<sup>1</sup>Athinoula A. Martinos Center for Biomedical Imaging, Department of Radiology, Massachusetts General Hospital, Harvard Medical School, Charlestown, MA, USA

<sup>2</sup>Department of Biochemistry and Biophysics, Perelman School of Medicine, University of Pennsylvania, Philadelphia, PA, USA

<sup>3</sup>Department of Chemistry, School of Arts and Sciences, University of Pennsylvania, Philadelphia, PA, USA

<sup>4</sup>Department of Biomedical Engineering, Boston University, Boston, MA, USA

<sup>5</sup>Department of Physics, Engineering Physics and Optics, Université Laval, QC, Canada

<sup>6</sup>Department of Physiology, University of Arizona, Tucson, AZ, USA

<sup>7</sup>Department of Neurosciences, University of California San Diego, La Jolla, CA, USA

<sup>8</sup>Department of Radiology, University of California San Diego, La Jolla, CA, USA

## Corresponding authors:

Sava Sakadžić, Athinoula A. Martinos Center for Biomedical Imaging, Massachusetts General Hospital, Harvard Medical School 149, 13th Street, Charlestown, MA 02129, USA.

Email: sava.sakadzic@mgh.harvard.edu

Anna Devor, Department of Biomedical Engineering, Boston University, Boston, MA 02215, USA.

Email: adevor@bu.edu

## Introduction

The cerebral cortex has a laminar structure, where neuronal circuits are organized into stratified subsurface layers.<sup>1–3</sup> It has been long hypothesized that cortical layers differ in their metabolic demand.<sup>4–6</sup> Indeed, at least in the primary sensory cortices, the laminar metabolic profile, as indicated by measurements of mitochondrial cytochrome c oxidase distribution, co-varies with vascular density and—to a lesser extent—the density of cell bodies.<sup>7–10</sup> Within these cortical regions, the highest cell density (of neurons and glia) is found in layer IV, and the lowest—in layer I.<sup>11</sup> Layer IV also has the highest density of cytochrome c oxidase, a marker of mitochondrial O<sub>2</sub> metabolism, and the highest density of microvasculature. Although both cytochrome c oxidase and microvascular density decrease from layer IV to layer I, this overall decrease is much more modest and gradual than the sharper decrease in the cell density at the transition between layer II and layer I. Vascular density correlates better with cytochrome c oxidase than cellular (and synaptic) density, and reports suggest that this stronger correlation may reflect a context-dependent cortical computation, where only a few of the neurons and synapses may be active at any given time,<sup>10</sup> and that microvascular density may be optimized to serve resting (idle) metabolic needs rather than rapid changes in metabolism driven by neuronal dynamics.<sup>12,13</sup>

In addition to the unresolved questions related to laminar differences in cortical O<sub>2</sub> delivery and consumption at rest, it is also not well understood how changes in O<sub>2</sub> delivery and consumption behave across cortical layers during functional activation. Previous studies using functional magnetic resonance imaging (fMRI) during neuronal activation have demonstrated laminar differences in both the change in cerebral blood flow ( $\Delta$ CBF)<sup>14–16</sup> and the blood oxygen level dependent (BOLD) fMRI signal,<sup>14,17–19</sup> further suggesting potentially different transient metabolic demands and oxygenation changes across cortical layers. However, additional more direct measurements of changes in the O<sub>2</sub> metabolism, vascular oxygenation, and blood flow in cortical layers are necessary to better understand laminar differences in O<sub>2</sub> demand transients and how vascular network supports them, as well as to improve the laminar fMRI BOLD signal interpretation. As a first step towards this goal, the present work addresses the laminar profile of vascular compartment-specific (arteriolar and venular) partial pressure of O<sub>2</sub> (pO<sub>2</sub>) changes across cortical layers in fully awake mice responding to sensory (whisker) stimulation.

Recently, we showed that heterogeneity of blood flow and capillary oxygenation decrease with increasing

cortical depth in awake mice at rest, reaching the minimum in layer IV.<sup>20</sup> These results suggest that oxygen transport to tissue is optimal where resting O<sub>2</sub> metabolism is presumably highest, supporting the idea of optimization governed by the resting metabolic needs. However, it remains not well understood how stimulus-induced responses in microvascular oxygenation differ across cortical layers. In the present work, we focus on the laminar profile of microvascular oxygenation changes during hemodynamic response to transient neuronal activation. The experiments were performed in healthy, awake mice (without anesthesia or sedation) using two-photon phosphorescence lifetime microscopy (2PLM)<sup>21,22</sup> in combination with a new oxygen probe Oxyphor 2P.<sup>23</sup> Surprisingly, our results indicate that changes in intravascular partial pressure of O<sub>2</sub> (pO<sub>2</sub>) are conserved across cortical layers I–IV, suggesting a tightly controlled neurovascular response that maintains adequate O<sub>2</sub> supply across the cortical layers. We also found that veins experience a more pronounced increase than arteries in oxygen saturation of hemoglobin in response to activation ( $\Delta$ sO<sub>2</sub>). Venous  $\Delta$ sO<sub>2</sub> also exhibited a progressive increase towards the cortical surface. In contrast to previous studies performed in anesthetized animals,<sup>24–26</sup> we did not observe the initial rapid decrease in intravascular pO<sub>2</sub> known as the “initial dip.” These findings are important for understanding layer-specific cortical metabolism and hemodynamic responses, and are of particular relevance for interpreting observations from fMRI studies, where individual cortical layers can be resolved.

## Methods

### Optical setup

Experiments were performed using a setup described previously in Sakadzic et al.<sup>27</sup> and Yaseen et al.,<sup>28</sup> which includes two-photon microscopy (2PM), optical coherence tomography (OCT), and optical intrinsic signal imaging (OISI) capabilities (Figure 1).

The OISI was used for mapping the center of cortical activation to identify the regions of interest (ROIs) for pO<sub>2</sub> measurements. 2PM was used for pO<sub>2</sub> measurements, acquisition of three-dimensional (3D) microvascular angiograms, and dynamic arteriolar diameter measurements. Spectral-domain OCT was used for measuring the axial component of red blood cell (RBC) velocity.<sup>30</sup>

### Animal subjects

All surgeries and experimental procedures were performed in accordance with the recommendations

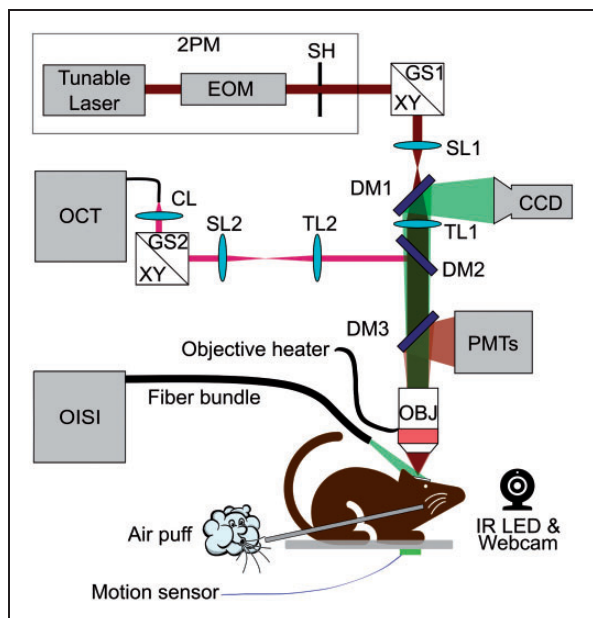


**Figure 1.** Schematic of the multi-modal optical imaging setup combining OISI, OCT, and 2PM. Tunable laser: femtosecond pulsed laser (680 nm–1300 nm); EOM: electro-optic modulator; SH: shutter; GS: XY galvanometer scanner; SL: scan lens; TL: tube lens; CL: collimation lens; DM: dichroic mirror; OBJ: microscope objective lens; PMTs: four-channel detector unit with photomultiplier tubes; CCD: charge-coupled device camera; OISI: optical intrinsic signal imaging; OCT: optical coherence tomography; 2PM: two-photon microscopy. For OISI: The cranial window was illuminated with green light ( $570 \pm 5$  nm) and reflection was collected by an objective (XLFluorx4, 4 $\times$ , 0.28 NA, Olympus). Images were recorded using a camera (CoolSNAPfx, Roper Scientific) controlled by custom-written software<sup>29</sup> in LabWindows CVI (National Instruments). For 2PM: Power and excitation gate duration of a femtosecond laser (680 nm–1300 nm, 80 MHz, Insight, Spectra-Physics) were controlled by an electro-optic modulator (350–160BK, ConOptics). The excitation beam was steered in X&Y dimensions by galvanometer-mirrors (6215HB, Cambridge Technologies). The beam was focused into the desired cortical layer via an objective lens (XLUMPLFLN-W, 20 $\times$ , 1.0 NA, Olympus). Emission was reflected by an epi-dichroic mirror (FF875-Di01-25  $\times$  36, Semrock Inc.) towards photomultiplier tubes (PMTs), located behind an infrared blocker (FF01-890/SP-50, Semrock Inc.). A photon counting PMT (HI0770PA-50, Hamamatsu) with an emission filter (FF01-795/150-25, Semrock Inc.) was used for detection of phosphorescence emission of Oxyphor 2P<sup>23</sup>. A second PMT, operated in analog mode (R3896, Hamamatsu) with an emission filter (FF01-525/50-25 or FF01-593/40-25 Semrock Inc.), was used for recording fluorescence emission from other vascular contrast agents. Custom software written in LabVIEW (National Instruments) was used for hardware control, synchronization, and data acquisition. For OCT: A superluminescent diode ( $1310 \pm 85$  nm, LSC2000C, Thorlabs Inc.) was used as the illumination source. The beam was steered by another pair of galvo-mirrors (6210H, Cambridge Technology), independently from the 2PM beam, which allowed simultaneous 2PM and OCT acquisitions. For detection, we used a line scan camera (Sensors Unlimited, Inc., 2048L and 2048R), operating at 50 kHz/Aline. Data were acquired by using custom software written in Qt C++ (The Qt Company).<sup>31</sup>

outlined in the Guide for the Care and Use of Laboratory Animals, approved by the Massachusetts General Hospital Subcommittee on Research and Animal Care (protocol number: 2007N000050), and reported in compliance with the ARRIVE guidelines (Animal Research: Reporting in Vivo Experiments). Animals were housed as cage mates of 2–4, under daily veterinary care, in 12/12 light/dark cycle with free access to food and water. We used 10 mice in this study (C57BL/6, 3–5 months old, female, weight = 20–25 g, Charles River Laboratories). We used only females because they exhibited less aggressive behavior and were easier to accustom to head restraint compared to males, and only young-adult animals because this study is a first step of ongoing and future research that will investigate different age groups, cortical regions, and pathological conditions. Two additional mice were prepared but not used due to complications: headpost touching the objective lens, dura thickening, and pial arteriolar hemorrhage. Experiments were performed during the daytime (9 am–7 pm) in a dark microscope enclosure.

### Chronic cranial window installation

Mice were injected with dexamethasone (4.8 mg/kg) and cefazolin (0.5 g/kg) 4–6 h before surgery to prevent brain edema and infection, respectively. Mice were anesthetized with isoflurane (2% induction, 1%–2% surgery). A circular skin incision was made on the scalp over the frontal and sagittal bone. Exposed periosteum was scraped by a No. 15 blade to ensure good fixation. To immobilize the animals later during imaging, a custom holding bar<sup>32</sup> was glued to the skull. A craniotomy (3 mm in diameter), with the dura left intact, was performed on the left hemisphere over primary somatosensory cortex (SI) (A–P: 2.0, L–R: 3.0 mm). The craniotomy was then sealed with a glass-plug<sup>33,34</sup> and dental cement. To prevent infection and pain, Sulfamethoxazole/Trimethoprim and Ibuprofen were supplied in drinking water for five days post-surgery, in addition to intraperitoneal injections of Cefazolin (0.05 mL) twice a day, and daily subcutaneous injections of Buprenorphine (0.05 mL). Pellets of food immersed in drinking water were also provided in a petri dish placed on the cage floor to ensure that mice remained well fed and hydrated.

### Training for awake imaging

After a week of recovery from surgery, mice were trained to accept head-fixation in the custom-designed cradle during imaging sessions up to 2 h. A reward (sweetened milk) was offered every  $\sim 15$  min during training and imaging sessions. The cradle and head-post were designed to minimize animal

discomfort. The animal was placed on a suspended fabric bed, free to display natural grooming behavior. Mouse behavior was monitored during experiments using a webcam (Microsoft LifeCam 6CH-0000) with removed infrared (IR) filter. The face and forepaws were illuminated with a light-emitting diode ( $\lambda = 940$  nm, Vishay TSAL6100), emission of which was passed through a long-pass filter (Thorlabs, FELH0900). Additionally, animal movement was recorded with an accelerometer sensor (ADXL335, 3-Axis Accelerometer) attached under the cradle. Experiments were terminated immediately if signs of elevated discomfort/anxiety were observed.

### *Functional activation protocol*

A Picospritzer microinjection device (051-0500-900, Parker Hannifin Inc.) was used to deliver air puffs (10–20 psi) for gentle stimulation of a whisker pad or shoulder—that have neighboring somatotopic representations in the primary somatosensory cortex to induce localized functional hyperemia. Air puffs were delivered to the contralateral side of the body, i.e. opposite from the brain hemisphere over which the cranial window was installed. For activation of the whisker barrel cortex, the air puffs were delivered from behind the whisker pad to avoid the eye blink reflex. The plastic tube that delivered the air was aimed at the E1 whisker, puffing from behind the mouse face and avoiding the eye, with the goal of optimizing reproducibility across imaging sessions and animals. Since we did not trim other whiskers, our stimulus affected multiple whiskers. For activation of the shoulder region, air puffs were delivered from the side, aiming directly at the shoulder. Inter-stimulation interval (ISI, onset-to-onset) was 25-s-long. Twenty stimulus trials (2 sessions, 10 repetitions in each) were presented for imaging at each cortical depth category. Each trial was composed of 5-s-long baseline, 2-s-long stimulation (3 Hz frequency, 1-ms-wide pulses to Picospritzer), and 18-s-long recovery.

### *Mapping the center of cortical activation*

The OISI module integrated in the multimodal microscope<sup>28</sup> was used to map the response to stimulation on the cortical surface in each animal. The intensity of diffusely reflected light, at wavelength near the isosbestic point for oxy- and deoxy-hemoglobin,<sup>35</sup> varied during brain activation mostly due to changes of the blood volume. This variation was recorded by the camera (6.8 fps) during the activation paradigm described above. Ratio images of activation were calculated by dividing the response (averaged during 0–2 s following the stimulus onset) by the baseline image

(averaged during 5 s before the stimulus). The center of activation was defined as a weighted centroid of the ratio map.

### *Delivery of molecular probes*

All dye solutions were prepared using 1× phosphate-buffered saline (Sigma Aldrich) and filtered through a 0.2  $\mu$ m filter (Acrodisc 4602, PALL) before administration. Animals were briefly (5–10 min) anesthetized using 1.5% isoflurane. The dye solutions (volumes of 0.10–0.15 mL) were injected retro-orbitally: Oxyphor 2P ( $\sim 6$  mg/mL) for intravascular pO<sub>2</sub> measurements, dextran-conjugated fluorescein isothiocyanate (FITC;  $\sim 8.3$  mg/mL, FD2000S, 2 MDa, Sigma Aldrich) for arteriolar diameter measurements, and Rhodamine B isothiocyanate–Dextran (80 mg/mL, R9379, 70 kDa, Sigma Aldrich) for angiograms. Animals regained consciousness within a few minutes and rested for 30–50 min before imaging sessions.

### *Data acquisition and analysis for intravascular pO<sub>2</sub> measurements*

The details regarding the synthesis and calibration of the Oxyphor 2P were described in Esipova et al.<sup>23</sup> Upon intravascular injection, Oxyphor 2P (molecular weight of  $\sim 75$  kDa) was retained within the vasculature and reported on the pO<sub>2</sub> in the blood plasma. Using the 2PM arm of the multimodal microscope, pO<sub>2</sub> in pre-selected locations was recorded using the following procedure: the laser beam was focused inside a vessel, the phosphorescence was excited by 10- $\mu$ s-long excitation gates ( $\lambda_{\text{ex}}=950$  nm), and the emission decay ( $\lambda_{\text{max}}=757$  nm) was acquired for 290  $\mu$ s immediately following the excitation. Based on our previous measurements, we estimate that our phosphorescence emitting volume at the focus was  $\sim 2$   $\mu$ m diameter in the lateral and  $\sim 5$   $\mu$ m in the axial dimension.<sup>22</sup> The photon counts were binned into 2- $\mu$ s-long bins. Typically,  $\sim 50$  photon counts were acquired after one excitation gate. Multiple decays were accumulated per pO<sub>2</sub> point measurement (50 decays  $\times$  3 repetitions = 150) with total acquisition time of 45 ms, unless otherwise noted. Starting 5  $\mu$ s after the excitation gate to minimize the influence of the instrument response function, the 285- $\mu$ s-long portion of the decay tail was fitted to a single-exponential, and the decay lifetime ( $\tau$ ) was converted into absolute pO<sub>2</sub> using a Stern–Volmer-like expression obtained during independent calibrations.<sup>36</sup> A heater (TC-HLS-05, Bioscience Tools) was used to keep the temperature of the water between the objective lens and cranial window at 37°C.

A field of view for  $pO_2$  measurement ( $\sim 600 \times 600 \mu m^2$ ) was selected within a 1-mm radius of the cortical activation center. At each imaging depth,  $pO_2$  measurements were performed in 7 diving arterioles and surfacing venules. Cycling through 7 locations took  $\sim 0.6$  s (including time for accumulation of the decays and galvo-mirror movement and settling between the locations), which determined the temporal resolution of our measurements. Data were acquired during the initial 18.6 s of the 25-s-long ISI, while the remaining 6.4 s of each ISI was used for data transfer and for rearming the microscope hardware. The mean baseline  $pO_2$  in penetrating arterioles and venules was estimated by averaging the  $pO_2$  values acquired along the same penetrating vessel trunks (11 arterioles, 14 venules) across  $n = 7$  mice; the same baseline data were used earlier in Li et al.<sup>20</sup>

$pO_2$  transients in individual vessels (Figure 3(c) and (d)) were measured by averaging up to 3000 phosphorescence decays per time point at each measurement location (50 decays  $\times$  3 repetitions  $\times$  10 trials  $\times$  2 sessions). At each measurement location,  $pO_2$  was measured every 0.6 s (1.67 Hz sampling rate) for 18.6 s during each stimulus trial. The mean  $pO_2$  across multiple penetrating venules and arterioles at each depth was computed. The mean  $\Delta pO_2$  transients were averaged across mice for each depth category. The  $\Delta pO_2$  extrema (the “overshoot” peak and the “undershoot” dip) were computed for each depth per animal by detecting the maximum between 0 and 4 s, and the minimum between 0 and 7 s after the stimulus onset. The mean and standard deviation of  $\Delta pO_2$  extrema across animals were calculated. The average  $\Delta pO_2$  at overshoot from all cortical depth categories per animal were statistically compared using Kruskal–Wallis test. The mean and standard deviation of  $\Delta pO_2$  transients (averaged across cortex per animal then across animals) during whisker versus shoulder stimulation were also calculated. All  $pO_2$ -related observables (e.g.,  $pO_2$ ,  $sO_2$ , and DOEF) and their changes due to stimulation were presented as absolute values (Figures 3 to 6 and Supplemental Figures 2 to 5).

The  $pO_2$  measurements during excessive animal motion were excluded from the data analysis ( $\sim 10\%$  of the measurements) based on a threshold criterion applied to the accelerometer recordings. The threshold ( $\Delta V = 36.5$  mV) was determined empirically by comparing the accelerometer readings during quiescent and movement periods as judged from the web cam data, as well as by observing large temporal changes in phosphorescence intensity due to displacement of the excitation volume outside the vessel. When the accelerometer reading exceeded the threshold at any time during a stimulus trial, the entire trial was rejected.

### Calculation of $sO_2$ and DOEF

Oxygen saturation ( $sO_2$ ) values were calculated from  $pO_2$  measurements based on the Hill equation with Hill coefficient values<sup>37</sup>— $h = 2.59$  and  $P_{50} = 40.2$  mmHg. The mean  $sO_2$  across multiple penetrating venules and arterioles were computed at each imaging depth. Subsequently, the mean  $\Delta sO_2$  transients were averaged across mice at each depth.

The  $\Delta sO_2$  extrema (overshoot peak and undershoot dip) for each depth were also calculated first in each animal, and then across animals. The average  $\Delta sO_2$  at overshoot in arterioles and in venules from all cortical depth categories per animal were statistically compared using Kruskal–Wallis test.

The depth-dependent oxygen extraction fraction (DOEF) at each cortical depth category was defined as the oxygen extraction fraction accumulated downstream from that depth:  $DOEF (\%) = (sO_{2,art} - sO_{2,ven}) / sO_{2,art} \times 100$ . Note that by this definition, pial DOEF represents the global OEF in the corresponding cortical region. Baseline DOEF was calculated at each cortical depth category per animal. Subsequently, the mean DOEF changes ( $\Delta DOEF$ ) from baseline across animals were computed for each depth.

### Blood flow measurements

In a subset of  $pO_2$  experiments (in  $n = 2$  mice), Doppler OCT was performed synchronously with 2PM to measure the change in the axial component of the blood flow speed during functional activation. The OCT B-scans (2048 A-lines, spanning 1 mm) were acquired during first 18.6 s of each ISI (2055 repeats). The axial components of blood flow velocities ( $V_z$ ) were calculated from the penetrating vessels,<sup>30</sup> which were identified using microvascular angiograms. The centroids of selected vessels were tracked across acquisitions during multiple ISIs. Small motion artifacts ( $< 20 \mu m$ ) were corrected by aligning vessel centroids, while the data that were substantially corrupted by the motion was excluded. The time traces were binned into 0.25-s-long bins and the average time trace within vessel boundaries was computed. Finally, the mean across multiple ISI acquisitions was calculated.

### Arteriolar diameter measurements

On separate days, the diameter change of the diving arterioles evoked by whisker stimulation was measured by 2PM. The blood plasma was labeled by FITC. In small ROIs centered at individual diving arterioles within the cortical activation region, two-dimensional raster scans were repeatedly acquired during the functional activation protocol (whisker stimulation). Arteriolar diameter changes ( $\Delta d$ ) were measured

50  $\mu\text{m}$  below the cortical surface in  $n=8$  mice, with 0.02 s temporal resolution from 2 to 5 arterioles per animal. A custom MATLAB (MathWorks Inc.) script was used to quantify the mean relative diameter change in response to functional activation for each animal.

### Microvascular morphology measurements

After all the functional measurements (e.g., intravascular  $p\text{O}_2$ , blood flow, and arteriolar diameter transients), on a separate day, we recorded microvascular angiograms within the same ROIs. 3D fluorescence intensity stacks were recorded in awake mice at rest, down to 600  $\mu\text{m}$  from the cortical surface.

## Results

### Mapping of the hemodynamic response

We first localized the functional activation areas within the cranial window of each mouse using OISI. Examples of cortical responses to whisker and shoulder activation are shown in Figure 2(a) and (b), locations and size of which are consistent with the literature.<sup>38</sup> The block-averaged time courses of the reflectance signal from the whisker (black line) and shoulder (green line) activation centers (average from an area of  $\sim 230 \times 230 \mu\text{m}^2$ ), detected during stimulation, are presented in Figure 2(c). The stimulation by a 2-s-long train of air-puffs caused a rapid transient drop ( $\sim 2\%$ ) in the detected light intensity due to increased absorption by hemoglobin associated with an increase in the blood volume. The intensity returned to the

baseline 2–3 s after the stimulus offset. Across  $n=7$  animals, the intensity drop at the peak of the response was  $2.0 \pm 0.5\%$  (mean  $\pm$  std) during whisker stimulation and  $1.5 \pm 0.3\%$  during shoulder stimulation. Based on the functional activation maps (Figure 2), we selected the ROIs over the active cortical regions (Figure 3(b)) for the subsequent measurements of the intravascular  $p\text{O}_2$  transients in response to the same types of stimulus.

### Quantification of intravascular $p\text{O}_2$

The phosphorescence lifetime of Oxyphor 2P is inversely proportional to the oxygen concentration in the environment (Figure 3(a)). Oxyphor 2P has 2-photon excitation and emission peaks at 950 nm and 757 nm, respectively, the phosphorescence quantum yield of 0.23 (in the absence of oxygen), 2-photon absorption cross section near 950 nm of  $\sim 600 \text{ GM}$ , and its phosphorescence decays are closely approximated by single-exponential functions. These properties have enabled measurement of  $p\text{O}_2$  in individual vessels (including capillaries) down to the cortical depth of 600  $\mu\text{m}$ , which is significantly deeper than the depths reachable with the predecessor probe PtP-C343.<sup>39,40</sup> The probe's properties were also instrumental for recording of the  $p\text{O}_2$  transients, enabling  $p\text{O}_2$  measurements with higher temporal resolution in larger numbers of microvascular segments. Using PtP-343, intravascular  $p\text{O}_2$  transients with satisfactory signal-to-noise ratios (SNR) could be obtained by averaging 3000–40,000 decays,<sup>25,41</sup> depending on the probe's concentration. At equivalent concentrations, Oxyphor 2P offers  $\sim 60\times$  improvement

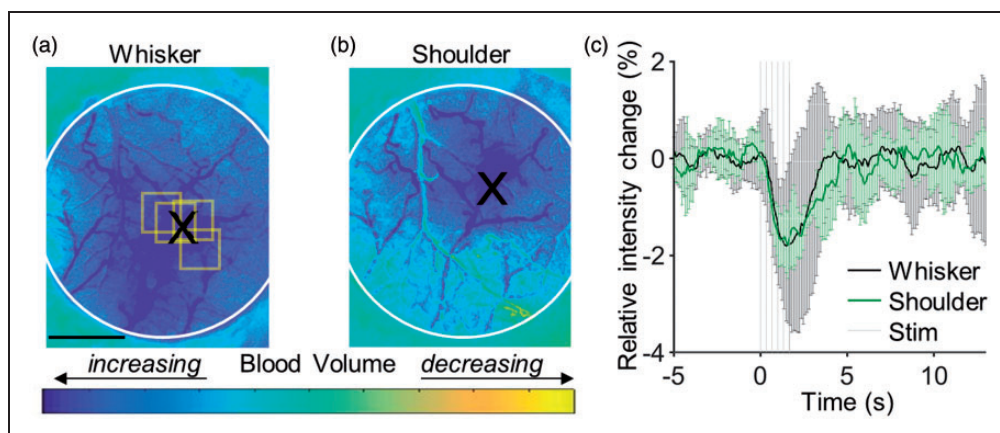


**Figure 2.** OISI mapping of the functional activation centers. Example ratio images during cortical activation in response to (a) whisker and (b) shoulder stimulation in an awake mouse. These ratio images were calculated relative to the pre-stimulus baseline (see Methods section). Dark blue areas indicate cortical regions with higher light absorption due to increased blood volume in response to stimulus-induced neuronal activity, centroids of which are marked with black “X” symbols. Yellow squares indicate the ROIs of  $p\text{O}_2$  measurements. The white circles in panels (a)–(c) delineate the cranial window. Scale bar: 1 mm. (c) The time course of trial-averaged responses at the whisker and shoulder activation centers. Error bars show standard deviation of relative intensity changes across repeated stimulus trials.

in the temporal resolution.<sup>23</sup> Although in this work we did not fully exploit the benefit of fast data acquisition, we confirmed, during the post-processing step, that adequate SNRs could have been obtained using on an average of only  $\sim 400$  decays per point (Supplemental Figure 1). Here, changes in local  $pO_2$  in response to 2-s-long whisker stimulation were measured in individual penetrating arterioles and venules by averaging  $\leq 3000$  decays per time point (Figure 3(c) and (d)). The measurements were performed at the cortical depth of  $350\ \mu\text{m}$  (Figure 3(b)). While the baseline  $pO_2$  values appeared heterogeneous (e.g., venule 4 and arteriole 7 in Figure 3(b) and (d)), the general profiles of stimulus-induced transients appeared consistent in all vessels. We also observed that baseline  $pO_2$  fluctuations in individual vascular segments were more pronounced in arterioles than in venules, likely because the

SNR of 2PLM  $pO_2$  measurements drops at higher  $pO_2$  values (Supplemental Figure 1).

We have previously observed that intravascular  $pO_2$  decreases with cortical depth in brains of awake mice, from the pial surface down to  $600\ \mu\text{m}$  depth, in both penetrating arterioles (from  $99 \pm 11\ \text{mmHg}$  to  $83 \pm 4\ \text{mmHg}$ ) and venules (from  $48 \pm 7\ \text{mmHg}$  to  $41 \pm 5\ \text{mmHg}$ ) (Figure 4(a)). Here, we investigated how the  $pO_2$  transients change in response to whisker stimulation as a function of cortical depth in layers I–Va (Figure 4(b) to (f)). Number of animals (n), arterioles, and venules that are measured at each cortical depth category (z) are given in Table 1.

The mean  $\Delta pO_2$  transients at different cortical depth categories are presented in Figure 4(b) and (c) (arteriolar and venular, respectively). The same plots, including the standard deviation bars together with the

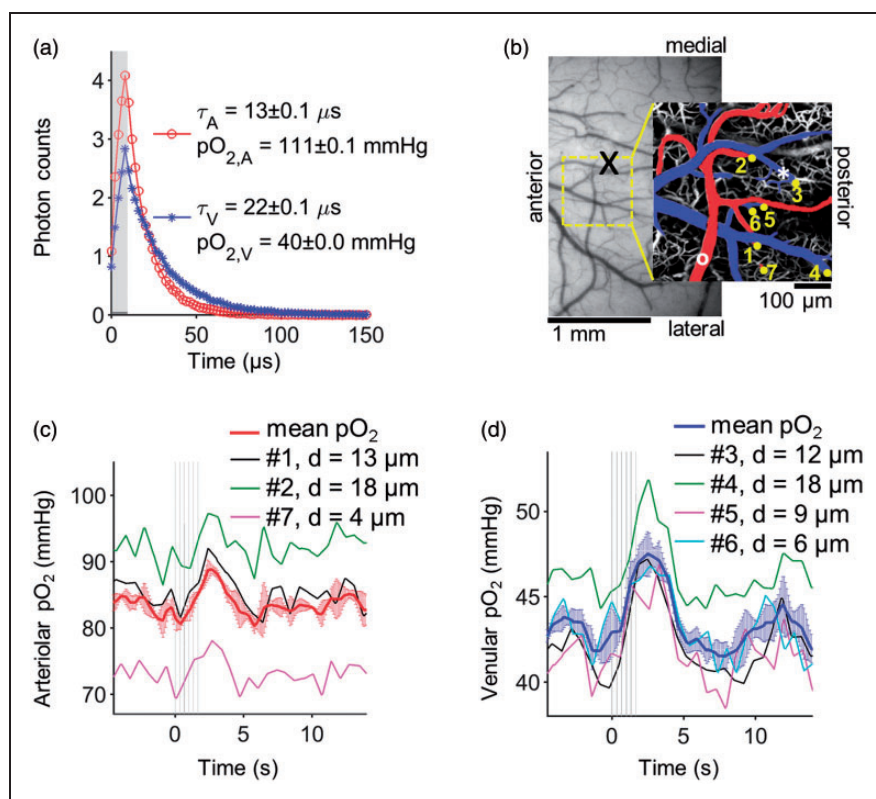


**Figure 3.** Measurements of  $pO_2$  transients in individual cortical arterioles and venules in response to whisker stimulation in awake mouse. (a) Examples of phosphorescence decays of Oxyphor 2P recorded at points within an arteriole (red line with circle symbols) and a venule (blue line with star symbols); the measurement locations are marked with a white circle and a white star in (b), respectively. The gray rectangle in (a) marks the phosphorescence excitation gate. The phosphorescence decay curves are averages of 1000 decays ( $50\ \text{decays} \times 10\ \text{trials} \times 2\ \text{sessions}$ ) that were measured at baseline. (b) CCD image of the cortical surface through the chronic glass-sealed cranial window. The centroid of activation region (mapped by using OISI) is marked with a black “X” symbol. The ROI selected for 2PM imaging is marked with a yellow-dashed square.  $pO_2$  was measured in the penetrating arterioles and venules diving at the locations marked with yellow dots, overlaid on a maximum intensity projection of a  $350\ \mu\text{m}$ -thick microvascular angiogram. The pial vessels are pseudo-colored in red (arterioles) and blue (venules). (c and d)  $pO_2$  transients in vessels 1–7 and their mean values at cortical depth of  $350\ \mu\text{m}$ . The diameter of each vessel (d) is indicated in legends. Error bars on the mean  $pO_2$  curves indicate standard deviation of  $pO_2$  across vessels. Air-puff timings for whisker stimulation are shown with light gray lines.  $pO_2$ : partial pressure of  $O_2$ .

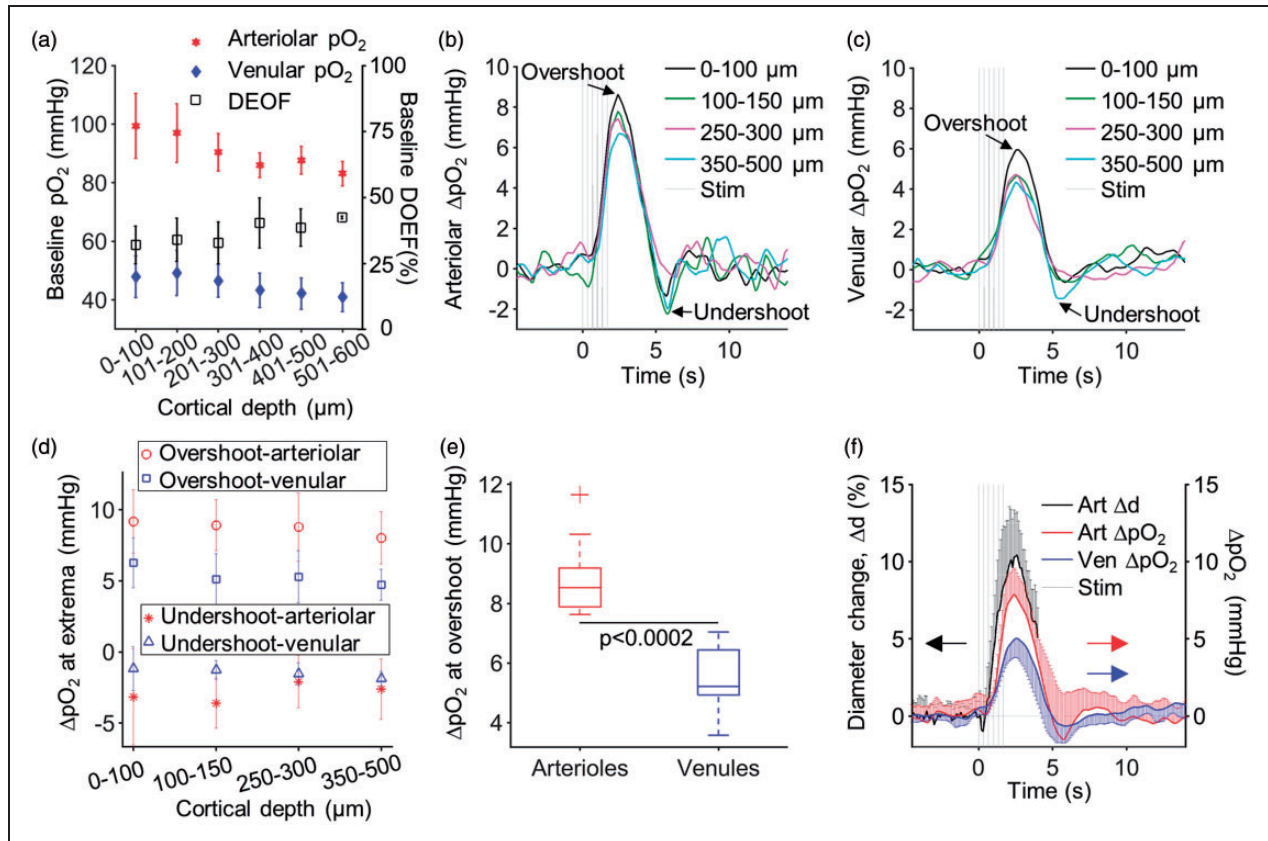


**Figure 4.** Arteriolar and venular pO<sub>2</sub> responses in awake mice across cortical layers I–IV. (a) Baseline pO<sub>2</sub> and DOEF in awake mice as a function of cortical depth. The change in arteriolar (b) and venular (c) pO<sub>2</sub> at different cortical depth categories in response to whisker stimulation. The measurements were averaged across  $n = 10$  mice at  $z = 0\text{--}100\ \mu\text{m}$ ,  $n = 9$  at  $z = 100\text{--}150\ \mu\text{m}$ ,  $n = 9$  at  $z = 250\text{--}300\ \mu\text{m}$ , and  $n = 7$  at  $z = 350\text{--}500\ \mu\text{m}$ . (d) The  $\Delta p\text{O}_2$  at extrema (e.g., post-stimulus overshoot and undershoot) in arterioles and in venules as a function of depth. (e) Boxplots of the  $\Delta p\text{O}_2$  values at overshoot in arterioles and venules from all cortical depths (Kruskal–Wallis,  $p = 0.0002$ ). The top and bottom edges of the boxes mark the 75th and 25th percentiles; the whiskers show the extreme ends of the data spread, excluding outliers (+ symbol), and the center lines mark the medians. (f) Comparison between the average arteriolar diameter changes, and the average arteriolar- and venular pO<sub>2</sub> change during functional activation. Arteriolar diameters were measured  $50\ \mu\text{m}$  below the cortical surface in  $n = 8$  mice. Arteriolar and venular pO<sub>2</sub> changes were first averaged within each depth range per animal and then averaged across animals. Error bars in panels (a), (d), and (f) are standard deviations across animals. They were plotted single-sided when their overlap impaired the visibility of multiple curves.

separately plotted responses from individual animals are provided in Supplemental Figure 2. In general, the overall shape of stimulus-induced  $\Delta p\text{O}_2$  transients was largely conserved across the measured depth range (cortical layers I–IV) and consisted of an initial increase (overshoot) followed by a decrease (undershoot) before returning to the baseline. The overshoot in the mean arteriolar  $\Delta p\text{O}_2$  at the surface reached the maximum of  $8.6 \pm 2.5$  mmHg at  $t = 2.4$  s, while at  $350\text{--}500\ \mu\text{m}$  below the surface the peak value was  $6.7 \pm 2.0$  mmHg at  $t = 2.5$  s (Figure 4(b)). Similarly, the overshoot in the mean venular  $\Delta p\text{O}_2$  at the surface reached the maximum of  $5.9 \pm 1.8$  mmHg at  $t = 2.6$  s, while at  $350\text{--}500\ \mu\text{m}$  below the surface the peak value was  $4.3 \pm 1.5$  mmHg at  $t = 2.5$  s (Figure 4(c)). We observed a small statistically non-significant trend of a reduced

$\Delta p\text{O}_2$  overshoot with increased cortical depth in both arterioles and venules. At all measured depths, the overshoot was followed by a post-stimulus undershoot (Figure 4(b) to (d)). The overshoots in arterioles, averaged across all cortical depths ( $8.9 \pm 1.3$  mmHg; mean  $\pm$  std; Figure 4(e)), were significantly larger than in venules ( $5.5 \pm 1.1$  mmHg; Figure 4(e)). However, the overshoot time-to-peak was largely invariant between arterioles ( $2.5 \pm 0.4$  s; mean  $\pm$  std) and venules ( $2.6 \pm 0.4$  s; mean  $\pm$  std). In contrast to previous studies under anesthesia, we did not observe the “initial dip” in our measurements. The undershoot was more pronounced and rapid in arterioles ( $3.1 \pm 2.2$  mmHg;  $4.5 \pm 0.2$  s; mean  $\pm$  std) compared to venules ( $1.5 \pm 0.7$  mmHg;  $5.4 \pm 0.9$  s), although this trend was not statistically significant. The baseline diameter values of all



**Table 1.** Number of animals (n), arterioles, and venules that are measured at each cortical depth category and corresponding layers.

Measurement	Cortical depth ( $\mu\text{m}$ )	Cortical layer	Number of animals (out of 10) <sup>a</sup>	Number of arterioles	Number of venules
<b>Whisker</b>					
Intrinsic signal	0–~400	I–IV	10	NA	NA
Partial pressure of oxygen	0–100	I	10	60	112
	100–150	II/III	9	50	100
	250–300	II/III	9	39	64
	350–500	IV, V <sub>a</sub> <sup>b</sup>	7	25	25
Diameter	50	I	8	26	0
Flow	0–300	I, II/III	2	0	2
<b>Shoulder</b>					
Intrinsic signal	0–~400	I–IV	7	NA	NA
Partial pressure of oxygen	0–100	I	5	19	29
	150	II/III	4	8	32
	300	II/III	3	8	22

<sup>a</sup>We pooled the data obtained from multiple recording sessions performed with the same animal. We considered measurements performed within the same subject dependent, and across subjects—independent.

<sup>b</sup>n = 6 in layer IV (320–450  $\mu\text{m}$ ) and n = 1 in layer V<sub>a</sub> (at 500  $\mu\text{m}$ ).

measured arterioles ( $13.1 \pm 7.3 \mu\text{m}$ , mean  $\pm$  std) and venules ( $12.3 \pm 6.4 \mu\text{m}$ , mean  $\pm$  std), from which  $p\text{O}_2$  response during function activation were extracted as a function of cortical depth, are shown in Supplemental Figures 3 and 4. Additionally, the stimulus-induced changes in arteriolar diameter were measured at cortical depth of  $z = 50 \mu\text{m}$  in  $n = 8$  mice. The mean arteriolar diameter increase was  $11.3 \pm 3.0\%$  from the baseline peaking at  $2.4 \pm 0.6$  s after the stimulus onset. To test whether this conserved behavior of the  $p\text{O}_2$  response can be generalized to other cortical regions, we applied the same stimulation paradigm to the shoulder area of SI. Our results indicate similar behavior of the mean  $\Delta p\text{O}_2$  transients in response to whisker and shoulder stimulation (Supplemental Figure 5).

### Quantification of $s\text{O}_2$

The mean arteriolar and venular  $\Delta s\text{O}_2$  transients at different cortical depths are presented in Figure 5(a) and (b), respectively. The mean  $s\text{O}_2$  during functional activation, averaged across all measured depths, increased in arterioles from  $90.4 \pm 1.9\%$  at baseline to  $92.0 \pm 1.5\%$  at the response peak, while the mean venular  $s\text{O}_2$  increased from  $58.4 \pm 5.5\%$  to  $64.8 \pm 4.1\%$  (Figure 5(g)). While the peak  $\Delta s\text{O}_2$  response in arterioles did not vary significantly with cortical depth ( $\Delta s\text{O}_2 = 1.6 \pm 0.4\%$  at the pial surface and  $1.8 \pm 0.7\%$  at 350–500  $\mu\text{m}$ ; Figure 5(c)), there was a trend of the  $\Delta s\text{O}_2$  overshoot amplitude decrease in venules as a function of cortical depth (from  $8.0 \pm 2.6\%$  at the pial surface to  $5.7 \pm 1.3\%$  at 350–500  $\mu\text{m}$ ). Since the hemoglobin in arterioles is nearly 100% oxygenated,

the arteriolar  $\Delta p\text{O}_2$  at the peak response corresponded to a significantly smaller arteriolar  $\Delta s\text{O}_2$  ( $< 2\%$ ) than the venular  $\Delta s\text{O}_2$  ( $\sim 6\%$ ) (Kruskal–Wallis,  $p = 0.0002$ ; Figure 5(d)). For each cortical depth category, we also calculated the depth-dependent oxygen extraction fraction (OEF) as  $\text{DOEF} = (s\text{O}_{2,\text{art}} - s\text{O}_{2,\text{ven}}) / s\text{O}_{2,\text{art}}$ . The DOEF exhibited a transient reduction from baseline in response to functional activation (Figure 5(e)), because the flow response was disproportionately larger than the increase in metabolic rate of oxygen, as expected during a healthy hemodynamic response.<sup>24</sup> A smaller DOEF reduction was observed at greater cortical depths (from  $35.7 \pm 0.5\%$  at the baseline to  $29.8 \pm 2.3\%$  at the peak of response; Figure 5(f)).

### Quantification of blood flow velocity

In a subset of experiments, we measured the absolute axial blood flow velocity in penetrating vessels simultaneously with  $p\text{O}_2$  (Figure 6). An example of such measurements in the same surfacing venule is presented in Figure 6(b). In Figure 6(c), we superimposed the mean venular velocity changes and absolute  $p\text{O}_2$  during functional activation ( $n = 2$ ). The venular blood flow velocity increased by  $\sim 25\%$  and preceded  $p\text{O}_2$  response by  $\sim 1$  s at half-maximum.

### Discussion

In this work, we used 2PLM in combination with a new oxygen probe Oxyphor 2P to investigate transient changes in intravascular  $p\text{O}_2$  in SI associated with neuronal response to sensory stimulation in awake mice. We demonstrated that stimulus-induced changes in  $p\text{O}_2$  along diving arterioles and surfacing venules are

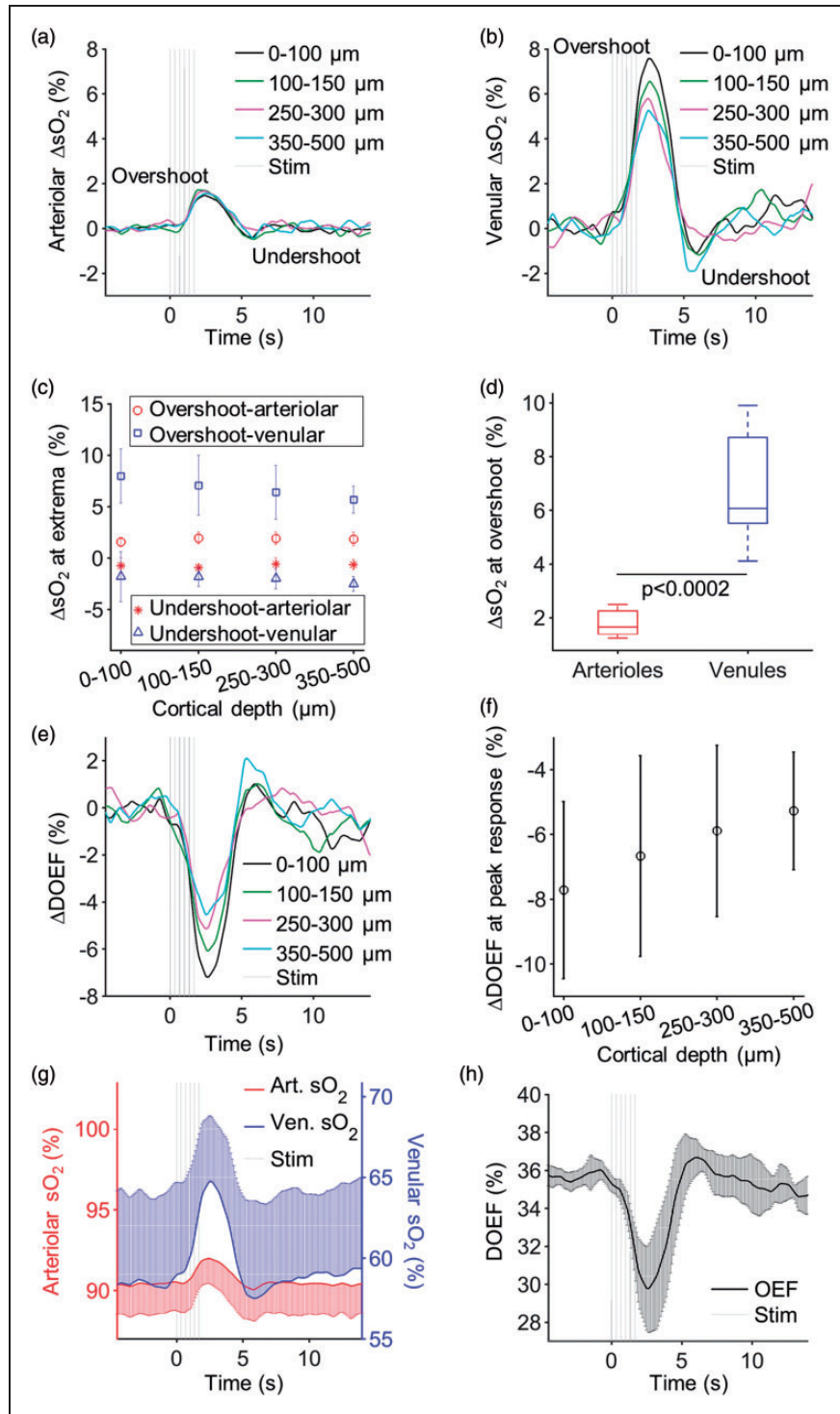


**Figure 5.** Arteriolar and venular  $sO_2$  responses and DOEF in awake mice across cortical layers I–IV. Average change in (a) arteriolar and (b) venular  $sO_2$  in response to functional activation at different cortical depth categories. (c) The  $\Delta sO_2$  at extrema (post-stimulus overshoot and undershoot) as a function of depth in arterioles and venules. (d) Boxplots of the  $\Delta sO_2$  values in arterioles and venules at overshoot from all cortical depths (0–100, 100–150, 250–300, and 350–500  $\mu m$ ) (Kruskal–Wallis,  $p = 0.0002$ ). The top and bottom edges of the boxes mark the 75th and 25th percentiles; the whiskers show the extreme ends of the data spread and the center lines mark the medians. (e) Average  $\Delta DOEF$  in response to functional activation at different cortical depth categories. (f) The  $\Delta DOEF$  at the peak of response as a function of cortical depth. (g) The mean arteriolar and venular  $sO_2$  during functional activation, averaged across all depths. (h) The mean DOEF transient during functional activation, averaged across all cortical depths. The error bars at (c), (f), (g), and (h) are showing the standard deviation across animals. Error bars are plotted only single sided when their overlap impaired the visibility of multiple curves.  $\Delta DOEF$ : change in depth-dependent oxygen extraction fraction.

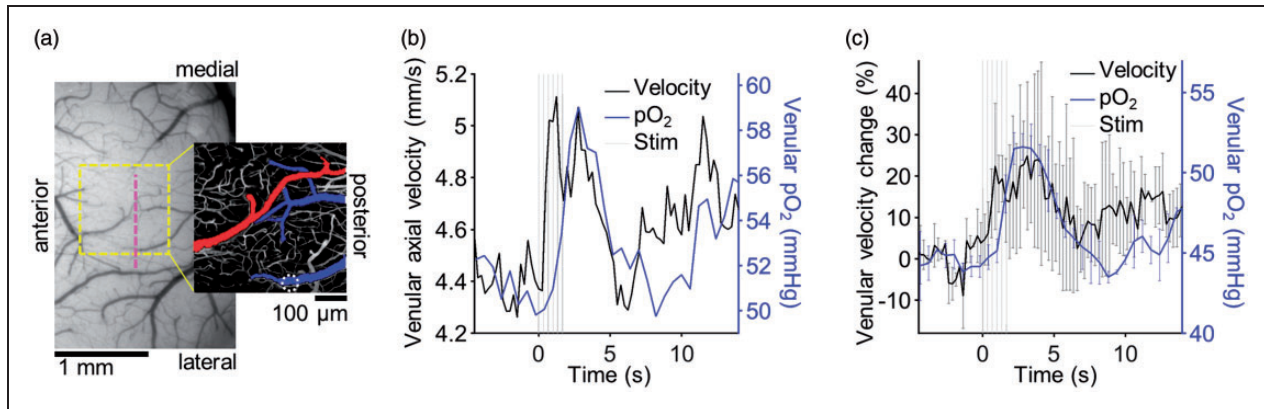


**Figure 6.** Simultaneous pO<sub>2</sub> and blood velocity measurements. (a) A CCD image of the cortical surface as seen through the chronic glass-sealed cranial window. The ROI selected for 2PM (for pO<sub>2</sub> measurements) is marked with a yellow square. Vertical dashed line marks the position of the Doppler OCT B-scan, used to measure the axial component of the blood velocity. The pial vessels are pseudo-colored (arterioles—red; venules—blue) on the maximum intensity projection of the 2PM angiogram, encompassing ~40  $\mu$ m depth. The white dashed circle marks the location of the surfacing venule from which simultaneous absolute pO<sub>2</sub> and velocity measurements are reported in (b). (c) Comparison between the percent change in axial component of the venular blood flow velocity and venular pO<sub>2</sub> during functional activation ( $n = 2$ ). Error bars in (c) show the velocity projection standard deviation across animals. pO<sub>2</sub>: partial pressure of O<sub>2</sub>.

largely invariant across the imaged depth (layers I–IV). In addition, we found (1) a larger increase in  $\Delta sO_2$  on the venous side compared to the arterial side, (2) a progressive increase in venous  $\Delta sO_2$  towards the cortical surface, and (3) absence of the intravascular “initial dip.”

Preservation of shape and amplitude of the  $\Delta pO_2$  response is expected along the diving arterioles where, in the awake state, the O<sub>2</sub> extraction ( $\Delta sO_2$ ) is small.<sup>20,39</sup> On the venous side, the interpretation is not as obvious, given some evidence that layer IV may experience higher stimulus-induced increase in blood flow and O<sub>2</sub> metabolism than layer I does. Below, we consider this evidence starting with the baseline conditions followed by dynamic increase due to neuronal activation.

At the baseline (i.e., during spontaneous neuronal activity in the absence of external stimulation), a body of evidence indicates that CBF is higher in layer IV than other layers. Our recent study indicates that the mean capillary RBC flux in layers IV and I are similar in the mouse primary somatosensory cortex.<sup>20</sup> However, capillary density in layer IV is almost twice as high as that in layer I.<sup>8,10,27</sup> Therefore, the total perfusion and blood volume in layer IV could also be twice as high as in layer I, which corroborates the results of an independent study in mice performed using OCT.<sup>42</sup> When considering O<sub>2</sub> metabolism, data comparing cortical layers are not available. It is known that neuronal cell body density as well as cytochrome oxidase density in layer IV are higher than these in layer I.<sup>8–11,43</sup> However, the question of whether these high neuronal

and cytochrome oxidase densities can be interpreted as evidence for high O<sub>2</sub> metabolism remains controversial.<sup>10</sup>

During stimulation, fMRI data in primates indicate that the change in  $\Delta CBF$ , quantified as a percent change from the baseline, is significantly higher in layer IV than in other layers.<sup>14–16</sup> Regarding stimulus-induced increase in O<sub>2</sub> metabolism, data comparing cortical layers have currently not been reported. Our present results demonstrating largely invariant  $\Delta pO_2$  across cortical layers I–VI suggest that higher  $\Delta CBF$  in layer IV is accompanied by higher increase in O<sub>2</sub> metabolism. In other words, the ratio of an increase in O<sub>2</sub> supply and demand associated with neuronal activation is conserved across cortical layers. Interestingly, we observed a small trend of progressive increase in venous  $\Delta sO_2$  towards the cortical surface, which apparently challenges our assertion of conserved ratio of O<sub>2</sub> supply and demand. However, this laminar difference in  $\Delta DOEF$ , which is only ~2.4% between layers IV ( $\Delta DOEF = -5.3 \pm 1.8\%$ ) and I ( $\Delta DOEF = -7.7 \pm 2.7\%$ ), could arise due to lower metabolism increase or presence of capillary thoroughfares in top cortical layers, resulting in highly oxygenated blood joining superficial draining venules.<sup>44,45</sup> In addition, the current study was limited to measurements along the main trunk of diving arterioles and surfacing venules, such that the  $\Delta DOEF$  at a certain depth reflected an accumulative extraction by cortical tissue below that depth. Although this way of measurements along the diving vessels is smearing the true laminar OEF profile, the rather modest laminar difference

in  $\Delta\text{DOEF}$  suggests a tightly controlled neurovascular response to ensure adequate  $\text{O}_2$  supply across cortical depth.

The feeding cortical arterioles have hemoglobin that is nearly saturated with oxygen ( $s\text{O}_{2,\text{art}} \approx 91\%$ ).<sup>20</sup> Therefore,  $\Delta s\text{O}_2$  in penetrating arterioles is small. In contrast, the venous baseline  $s\text{O}_2$  on the surface is low ( $s\text{O}_{2,\text{ven}} \approx 62\%$ )<sup>20</sup> and it increases significantly during the hemodynamic response. Similar trend of significantly larger  $s\text{O}_2$  change in venules than in arterioles was observed in the small emerging venules and pre-penetrating arterioles at the cortical surface of anesthetized rats during forepaw stimulation ( $\Delta s\text{O}_2 = 10.6 \pm 7.7\%$  and  $\Delta s\text{O}_2 = 4.3 \pm 9.6\%$ , respectively).<sup>46</sup> The stimulus-induced influx of oxygenated blood into the venous compartment provides the principal mechanism for the BOLD-fMRI contrast.<sup>47–49</sup> Specifically, in areas that experience an increase in neuronal activity, CBF increases much more than cerebral metabolic rate of oxygen ( $\text{CMRO}_2$ ), leading to the transient washout of the deoxygenated blood that drives the BOLD fMRI signal up. Previously, using the same 2PLM technique, we provided experimental data in support of the idea that the increase in blood oxygenation during the hemodynamic response, which has been perceived as a paradox,<sup>50,51</sup> may serve to prevent a sustained oxygenation drop at tissue locations remote from the vascular feeding sources.<sup>24</sup> The current study provides direct and quantitative experimental evidence of a larger increase in  $\Delta s\text{O}_2$  in surfacing venules compared to diving arterioles in awake mice.

The biphasic shape of the  $p\text{O}_2$  response—the initial overshoot followed by an undershoot before returning to baseline—was observed on both the arteriolar and venous side and was accompanied by the observed changes in arteriolar diameters. The latter is in agreement with our previous observations.<sup>19,52,53</sup> The presence of  $p\text{O}_2$  undershoot on the arterial side also argues against the possibility of its metabolic origin.<sup>54</sup> Indeed, if elevated  $\text{CMRO}_2$  lasted beyond the duration of dilation and CBF increase, the undershoot would appear on the venous and not arterial side. The biphasic shape of the  $p\text{O}_2$  response, as well as the observed progressive increase in venous  $\Delta s\text{O}_2$  towards the cortical surface during the stimulus-induced overshoot in  $p\text{O}_2$ , is consistent with previous layer-resolved BOLD fMRI studies by ourselves and others, which documented a biphasic BOLD signal with progressively increasing overshoot amplitude towards the cortical surface.<sup>14,16–19</sup> Our findings provide a quantitative insight into one component of the BOLD signal (e.g., hemoglobin saturation) and suggest that in combination with the more direct measurements of laminar CBF and  $\text{O}_2$  metabolism changes during activation, our measurements of laminar intravascular oxygenation

may be successfully applied to better understand the laminar fMRI BOLD signal.

Our measurements show that intravascular  $p\text{O}_2$  does not decrease prior to the overshoot—the phenomenon known as the “initial dip.”<sup>55,56</sup> The lack of the initial dip suggests that in awake mice the onset of arteriolar dilation occurs so fast, that the local changes in the blood plasma oxygenation are negligible, i.e. below  $\Delta p\text{O}_2 = 0.2 \text{ mmHg}$  (Supplemental Figure 1). Previously, using 2PLM, we have detected small initial dip ( $\sim 1 \text{ mmHg}$ ) in tissue  $p\text{O}_2$  in response to sensory stimulation under anesthesia.<sup>24</sup> It remains to be determined if the initial dip in tissue  $p\text{O}_2$  can be detected under awake conditions, where the CBF kinetics is faster.<sup>57–59</sup> In addition, the temporal resolution in our experiments was 0.6 s and it prevented us from measuring faster  $p\text{O}_2$  transients. If the initial dip occurs on a much faster time scale, it could have been missed by our measurements. We plan to address such possibilities in future studies by using advances in our optical methods that will enable improved temporal resolution with minimal trade-off in throughput.

Stimulus-induced increase in  $p\text{O}_2$  in surface arterioles peaked at 2.4 s followed by deeper arterioles and venules (2.5 s) and finally surface venules (2.6 s). However, these timing differences were not statistically significant, likely due to short transient times in the mouse cortex, and mixing of short and longer microvascular paths,<sup>60</sup> as well as our limited temporal resolution. A similar trend in temporal  $p\text{O}_2$  responses and lack of intravascular initial  $p\text{O}_2$  dip were previously reported at the cortical surface in response to forepaw stimulation in anesthetized rats.<sup>46</sup> We also observed that the venular  $p\text{O}_2$  transients were delayed by  $\sim 1 \text{ s}$  relative to the flow transients. Since most microscopic studies show small or no venular dilation in response to functional activation,<sup>61,62</sup> the velocity changes that we measured in veins are expected to relatively closely follow changes in flow. Although the temporal resolution of our  $p\text{O}_2$  measurements in an individual stimulation cycle was  $\sim 0.6 \text{ s}$ , we were able to observe these fine time differences in mean  $p\text{O}_2$  transients by jittering timing of acquisition (see Methods section). This temporal resolution may not have been sufficient to detect some faster temporal dynamics<sup>63</sup> or to significantly differentiate the time-to-peak differences between vessel types and cortical depths.

The superior properties of Oxyphor 2P enabled faster data acquisition and deeper sampling of cortical oxygenation than previously possible. In a recent study, we used Oxyphor 2P for imaging the resting intravascular oxygenation down to  $600 \mu\text{m}$  below the cortical surface, i.e., cortical layers I–V.<sup>20</sup> The present study is the first example applying Oxyphor 2P for recording of transient intravascular  $p\text{O}_2$  changes

associated with the hemodynamic response due to changes in neuronal activity. The optical deterioration with depth affects the baseline and functional  $pO_2$  measurements alike, resulting in a smaller percent of measurements from deeper locations with suitable signal to noise ratio. In addition, dynamic measurements are more susceptible to errors induced by mouse motion. This is because the measurements during response time-course are affected by both motion artifacts and movement-induced hemodynamic changes. In the present study, the combination of optical deterioration and motion artifacts has limited our measurements to cortical layers I–IV.

Most previous studies that used 2PLM for studying of the hemodynamic response have been conducted using animals under anesthesia. However, anesthesia affects neuronal activity as well as blood flow and oxygen metabolism, altering neurovascular and metabolic coupling. Physiological effects of different anesthesia methods have been well documented.<sup>39,59,64–74</sup> A number of compromises have been proposed involving light sedation.<sup>75</sup> However, our recent study shows that some of these sedation methods still have profound effects on the hemodynamic response kinetics.<sup>33</sup> Thus, the most effective approach may be stepping away from anesthesia altogether.<sup>20,33,39,42,65</sup> All measurements presented here were performed in awake mice in the absence of anesthesia or sedation.

Another important physiological factor is temperature. We maintained temperature of the immersion water between the tip of the objective lens and cranial window at 37°C during our measurements. Such tight control of temperature at the measurement site was critical, since temperature alters several parameters, including  $O_2$  diffusion and solubility in plasma, hemoglobin affinity to  $O_2$ , the triplet decay time of the oxygen probe, CBF, and  $CMRO_2$ .<sup>21,71,76–84</sup>

Taken together, our results indicate that the vascular structure and neurovascular coupling work in tandem to enable efficient and balanced  $O_2$  supply across the cortical depth answering metabolic needs, not only at rest but also during response to rapid changes in metabolism driven by transient neuronal dynamics. In the future, we will extend our 2PLM methodology to image tissue  $pO_2$  in awake mice for direct estimation of  $CMRO_2$ <sup>85</sup> across cortical layers.

#### Authors' note

Tatiana Esipova is now affiliated to Department of Chemistry and Biochemistry, Loyola University, Chicago, IL, USA.

Baoqiang Li is now affiliated to Brain Cognition and Brain Disease Institute, Shenzhen Institutes of Advanced Technology, Chinese Academy of Sciences; Shenzhen-Hong

Kong Institute of Brain Science, Shenzhen Fundamental Research Institutions, Shenzhen, China.

Mohammad A Yaseen is now affiliated to Department of Bioengineering, Northeastern University, Boston, MA.

#### Funding

The author(s) disclosed receipt of the following financial support for the research, authorship, and/or publication of this article: This study was supported by the National Institutes of Health grants K99MH120053, K99EB023993, R01NS091230, R01MH117359, P01NS055104, R01AA027097, R56AG058849, U24EB028941, R24NS092986, and U01HL133362.

#### Acknowledgements

The authors thank Mr. Rajeshwer Jaswal for his valuable help with the data processing related to the vascular diameter changes during functional activation.

#### Declaration of conflicting interests


The author(s) declared no potential conflicts of interest with respect to the research, authorship, and/or publication of this article.

#### Authors' contributions

İŞ designed and executed the experiments, processed data, and performed statistical analysis. KK and MD developed surgical and animal handling methods. TE and SAV developed and provided oxygen probe. BL helped with experiments. JEP and SK helped with data processing. MAY, SS, and HW developed and maintained the custom optical setup. BF and KK performed surgical preparations. SS, AD, and DAB conceived and guided the project. All authors contributed to the data interpretation. İŞ wrote the manuscript with help from AD, SS, TWS, and all other authors.

#### ORCID iDs

İkbal Şencan  <https://orcid.org/0000-0002-2903-041X>

Timothy W Secomb  <https://orcid.org/0000-0002-0176-5502>

#### Supplemental material

Supplemental material for this article are available online.

#### References

1. Feldmeyer D, Brecht M, Helmchen F, et al. Barrel cortex function. *Prog Neurobiol* 2013; 103: 3–27.
2. Harris KD and Shepherd GM. The neocortical circuit: themes and variations. *Nat Neurosci* 2015; 18: 170–181.
3. Helmstaedter M, de Kock CP, Feldmeyer D, et al. Reconstruction of an average cortical column in silico. *Brain Res Rev* 2007; 55: 193–203.
4. Devor A, Hillman EM, Tian P, et al. Stimulus-induced changes in blood flow and 2-deoxyglucose uptake dissociate in ipsilateral somatosensory cortex. *J Neurosci* 2008; 28: 14347–14357.

5. Tootell RB, Hamilton SL, Silverman MS, et al. Functional anatomy of macaque striate cortex. I. Ocular dominance, binocular interactions, and baseline conditions. *J Neurosci* 1988; 8: 1500–1530.
6. Weber B, Fouad K, Burger C, et al. White matter glucose metabolism during intracortical electrostimulation: a quantitative [ $^{18}\text{F}$ ]fluorodeoxyglucose autoradiography study in the rat. *NeuroImage* 2002; 16: 993–998.
7. Adams DL, Piserchia V, Economides JR, et al. Vascular supply of the cerebral cortex is specialized for cell layers but not columns. *Cereb Cortex* 2015; 25: 3673–3681.
8. Blinder P, Tsai PS, Kaufhold JP, et al. The cortical angiome: an interconnected vascular network with non-columnar patterns of blood flow. *Nat Neurosci* 2013; 16: 889–897.
9. Hirsch S, Reichold J, Schneider M, et al. Topology and hemodynamics of the cortical cerebrovascular system. *J Cereb Blood Flow Metab* 2012; 32: 952–967.
10. Weber B, Keller AL, Reichold J, et al. The microvascular system of the striate and extrastriate visual cortex of the macaque. *Cereb Cortex* 2008; 18: 2318–2330.
11. Keller D, Erö C and Markram H. Cell densities in the mouse brain: a systematic review. *Front Neuroanat* 2018; 12: 83.
12. Merkle CW and Srinivasan VJ. Laminar microvascular transit time distribution in the mouse somatosensory cortex revealed by Dynamic Contrast Optical Coherence Tomography. *NeuroImage* 2016; 125: 350–362.
13. Schmid F, Tsai PS, Kleinfeld D, et al. Depth-dependent flow and pressure characteristics in cortical microvascular networks. *PLoS Comput Biol* 2017; 13: e1005392.
14. Goense J, Merkle H and Logothetis NK. High-resolution fMRI reveals laminar differences in neurovascular coupling between positive and negative BOLD responses. *Neuron* 2012; 76: 629–639.
15. Zappe AC, Pfeuffer J, Merkle H, et al. The effect of labeling parameters on perfusion-based fMRI in nonhuman primates. *J Cereb Blood Flow Metab* 2008; 28: 640–652.
16. Guidi M, Huber L, Lampe L, et al. Lamina-dependent calibrated BOLD response in human primary motor cortex. *NeuroImage* 2016; 141: 250–261.
17. Siero JC, Hendrikse J, Hoogduin H, et al. Cortical depth dependence of the BOLD initial dip and poststimulus undershoot in human visual cortex at 7 Tesla. *Magn Reson Med* 2015; 73: 2283–95.
18. Silva AC and Koretsky AP. Laminar specificity of functional MRI onset times during somatosensory stimulation in rat. *Proc Natl Acad Sci U S A* 2002; 99: 15182–15187.
19. Tian P, Teng IC, May LD, et al. Cortical depth-specific microvascular dilation underlies laminar differences in blood oxygenation level-dependent functional MRI signal. *Proc Natl Acad Sci* 2010; 107: 15246–15251.
20. Li B, Esipova TV, Sencan I, et al. More homogeneous capillary flow and oxygenation in deeper cortical layers correlate with increased oxygen extraction. *eLife* 2019; 8: e42299.
21. Finikova OS, Lebedev AY, Aprelev A, et al. Oxygen microscopy by two-photon-excited phosphorescence. *ChemPhysChem* 2008; 9: 1673–1679.
22. Sakadzic S, Roussakis E, Yaseen MA, et al. Two-photon high-resolution measurement of partial pressure of oxygen in cerebral vasculature and tissue. *Nat Methods* 2010; 7: 755–759.
23. Esipova TV, Barrett MJP, Erlebach E, et al. Oxyphor 2P: a high-performance probe for deep-tissue longitudinal oxygen imaging. *Cell Metab* 2019; 29: 736–744.e7.
24. Devor A, Sakadžić S, Saisan PA, et al. “Overshoot” of  $\text{O}_2$  is required to maintain baseline tissue oxygenation at locations distal to blood vessels. *J Neurosci* 2011; 31: 13676–13681.
25. Lecoq J, Parpaleix A, Roussakis E, et al. Simultaneous two-photon imaging of oxygen and blood flow in deep cerebral vessels. *Nat Med* 2011; 17: 893–898.
26. Parpaleix A, Houssen YG and Charpak S. Imaging local neuronal activity by monitoring  $\text{pO}_2$  transients in capillaries. *Nat Med* 2013; 19: 241–246.
27. Sakadzic S, Mandeville ET, Gagnon L, et al. Large arteriolar component of oxygen delivery implies a safe margin of oxygen supply to cerebral tissue. *Nat Commun* 2014; 5: 5734.
28. Yaseen MA, Srinivasan VJ, Gorczynska I, et al. Multimodal optical imaging system for in vivo investigation of cerebral oxygen delivery and energy metabolism. *Biomed Opt Express* 2015; 6: 4994–5007.
29. Dunn AK, Devor A, Bolay H, et al. Simultaneous imaging of total cerebral hemoglobin concentration, oxygenation, and blood flow during functional activation. *Opt Lett* 2003; 28: 28–30.
30. Srinivasan VJ, Sakadžić S, Gorczynska I, et al. Quantitative cerebral blood flow with Optical Coherence Tomography. *Opt Express* 2010; 18: 2477–2494.
31. Wang H, Akkin T, Magnain C, et al. Polarization sensitive optical coherence microscopy for brain imaging. *Opt Lett* 2016; 41: 2213–2216.
32. Mateo C, Avermann M, Gentet LJ, et al. In vivo optogenetic stimulation of neocortical excitatory neurons drives brain-state-dependent inhibition. *Curr Biol* 2011; 21: 1593–1602.
33. Desjardins M, Kılıç K, Thunemann M, et al. Awake mouse imaging: from two-photon microscopy to blood oxygen-level dependent functional magnetic resonance imaging. *Biol Psychiatry Cogn Neurosci Neuroimaging* 2019; 4: 533–542.
34. Goldey GJ, Roumis DK, Glickfeld LL, et al. Removable cranial windows for long-term imaging in awake mice. *Nat Protoc* 2014; 9: 2515–2538.
35. Prahl S. Optical absorption of hemoglobin, <https://omlc.org/spectra/hemoglobin/> (1999, accessed 25 November 2018).
36. Esipova TV and Vinogradov SA. Synthesis of phosphorescent asymmetrically  $\pi$ -extended porphyrins for two-photon applications. *J Org Chem* 2014; 79: 8812–8825.
37. Uchida K, Reilly MP and Asakura T. Molecular stability and function of mouse hemoglobins. *Zool Sci* 1998; 15: 703–706.

38. Mohajerani MH, Chan AW, Mohsenvand M, et al. Spontaneous cortical activity alternates between motifs defined by regional axonal projections. *Nat Neurosci* 2013; 16: 1426–1435.
39. Lyons DG, Parpaleix A, Roche M, et al. Mapping oxygen concentration in the awake mouse brain. *eLife* 2016; 5: e12024.
40. Sakadžić S, Mandeville ET, Gagnon L, et al. Large arteriolar component of oxygen delivery implies a safe margin of oxygen supply to cerebral tissue. *Nat Commun* 2014; 5: 5734.
41. Moeini M, Lu X, Avti PK, et al. Compromised microvascular oxygen delivery increases brain tissue vulnerability with age. *Sci Rep* 2018; 8: 8219.
42. Merkle CW, Zhu J, Bernucci MT, et al. Dynamic Contrast Optical Coherence Tomography reveals laminar microvascular hemodynamics in the mouse neocortex in vivo. *NeuroImage* 2019; 202: 116067.
43. Tsai PS, Kaufhold JP, Blinder P, et al. Correlations of neuronal and microvascular densities in murine cortex revealed by direct counting and colocalization of nuclei and vessels. *J Neurosci* 2009; 29: 14553–14570.
44. Gutiérrez-Jiménez E, Cai C, Mikkelsen IK, et al. Effect of electrical forepaw stimulation on capillary transit-time heterogeneity (CTH). *J Cereb Blood Flow Metab* 2016; 36: 2072–2086.
45. Hudetz AG, Fehér G and Kampine JP. Heterogeneous autoregulation of cerebrocortical capillary flow: evidence for functional thoroughfare channels? *Microvasc Res* 1996; 51: 131–136.
46. Vazquez AL, Fukuda M, Tasker ML, et al. Changes in cerebral arterial, tissue and venous oxygenation with evoked neural stimulation: implications for hemoglobin-based functional neuroimaging. *J Cereb Blood Flow Metab* 2010; 30: 428–439.
47. Brown GG, Perthen JE, Liu TT, et al. A primer on functional magnetic resonance imaging. *Neuropsychol Rev* 2007; 17: 107–25.
48. Kwong KK, Belliveau JW, Chesler DA, et al. Dynamic magnetic resonance imaging of human brain activity during primary sensory stimulation. *Proc Natl Acad Sci U S A* 1992; 89: 5675–5679.
49. Ogawa S, Tank DW, Menon R, et al. Intrinsic signal changes accompanying sensory stimulation: functional brain mapping with magnetic resonance imaging. *Proc Natl Acad Sci* 1992; 89: 5951–5955.
50. Paulson OB, Hasselbalch SG, Rostrup E, et al. Cerebral blood flow response to functional activation. *J Cereb Blood Flow Metab* 2010; 30: 2–14.
51. Raichle ME and Mintun MA. Brain work and brain imaging. *Annu Rev Neurosci* 2006; 29: 449–476.
52. Devor A, Tian P, Nishimura N, et al. Suppressed neuronal activity and concurrent arteriolar vasoconstriction may explain negative blood oxygenation level-dependent signal. *J Neurosci Off J Soc Neurosci* 2007; 27: 4452–4459.
53. Uhlírova H, Kılıç K, Tian P, et al. The roadmap for estimation of cell-type-specific neuronal activity from non-invasive measurements. *Philos Trans R Soc Lond B Biol Sci* 2016; 371: 20150356.
54. Yucel MA, Devor A, Akin A, et al. The possible role of CO(2) in producing a post-stimulus CBF and BOLD undershoot. *Front Neuroenergetics* 2009; 1: 7.
55. Buxton RB. The elusive initial dip. *NeuroImage* 2001; 13: 953–958.
56. Vanzetta I and Grinvald A. Evidence and lack of evidence for the initial dip in the anesthetized rat: implications for human functional brain imaging. *Neuroimage* 2001; 13: 959–967.
57. Martin C, Martindale J, Berwick J, et al. Investigating neural-hemodynamic coupling and the hemodynamic response function in the awake rat. *Neuroimage* 2006; 32: 33–48.
58. Moeini M, Lu X, Bélanger S, et al. Cerebral tissue pO<sub>2</sub> response to stimulation is preserved with age in awake mice. *Neurosci Lett* 2019; 699: 160–166.
59. Pisauro MA, Dhruv NT, Carandini M, et al. Fast hemodynamic responses in the visual cortex of the awake mouse. *J Neurosci* 2013; 33: 18343–18351.
60. Li J, Bravo DS, Upton AL, et al. Close temporal coupling of neuronal activity and tissue oxygen responses in rodent whisker barrel cortex. *Eur J Neurosci* 2011; 34: 1983–1996.
61. Drew PJ, Shih AY and Kleinfeld D. Fluctuating and sensory-induced vasodynamics in rodent cortex extend arteriole capacity. *Proc Natl Acad Sci U S A* 2011; 108: 8473–8478.
62. Hillman EMC, Devor A, Bouchard MB, et al. Depth-resolved optical imaging and microscopy of vascular compartment dynamics during somatosensory stimulation. *NeuroImage* 2007; 35: 89–104.
63. Secomb TW, Bullock KV, Boas DA, et al. The mass transfer coefficient for oxygen transport from blood to tissue in cerebral cortex. *J Cereb Blood Flow Metab*. Epub ahead of print 18 August 2019. DOI: 10.1177/0271678X19870068.
64. Aksenov DP, Li L, Miller MJ, et al. Effects of anesthesia on BOLD signal and neuronal activity in the somatosensory cortex. *J Cereb Blood Flow Metab* 2015; 35: 1819–1826.
65. Cao R, Li J, Ning B, et al. Functional and oxygen-metabolic photoacoustic microscopy of the awake mouse brain. *NeuroImage* 2017; 150: 77–87.
66. Ciobanu L, Reynaud O, Uhrig L, et al. Effects of anesthetic agents on brain blood oxygenation level revealed with ultra-high field MRI. *PLoS One* 2012; 7: e32645.
67. Fish R, Danneman PJ, Brown M, et al. *Anesthesia and analgesia in laboratory animals*. Cambridge: Academic Press, 2011.
68. Masamoto K, Fukuda M, Vazquez A, et al. Dose-dependent effect of isoflurane on neurovascular coupling in rat cerebral cortex. *Eur J Neurosci* 2009; 30: 242–250.
69. Nakao Y, Itoh Y, Kuang T-Y, et al. Effects of anesthesia on functional activation of cerebral blood flow and metabolism. *Proc Natl Acad Sci* 2001; 98: 7593–7598.
70. Park K, Chen W, Volkow ND, et al. Hemodynamic and neuronal responses to cocaine differ in awake versus

- anesthetized animals: optical brain imaging study. *NeuroImage* 2019; 188: 188–197.
71. Roche M, Chaigneau E, Rungta RL, et al. In vivo imaging with a water immersion objective affects brain temperature, blood flow and oxygenation. *eLife* 2019; 8: e47324.
  72. Seto A, Taylor S, Trudeau D, et al. Induction of ischemic stroke in awake freely moving mice reveals that isoflurane anesthesia can mask the benefits of a neuroprotection therapy. *Front Neuroenergetics* 2014; 6: 1.
  73. Thrane AS, Rangroo Thrane V, Zeppenfeld D, et al. General anesthesia selectively disrupts astrocyte calcium signaling in the awake mouse cortex. *Proc Natl Acad Sci U S A* 2012; 109: 18974–18979.
  74. Tran CHT and Gordon GR. Astrocyte and microvascular imaging in awake animals using two-photon microscopy. *Microcirculation* 2015; 22: 219–227.
  75. Sharp PS, Shaw K, Boorman L, et al. Comparison of stimulus-evoked cerebral hemodynamics in the awake mouse and under a novel anesthetic regime. *Sci Rep* 2015; 5: 12621.
  76. Benesch R and Benesch RE. Intracellular organic phosphates as regulators of oxygen release by haemoglobin. *Nature* 1969; 221: 618–622.
  77. Croughwell N, Smith LR, Quill T, et al. The effect of temperature on cerebral metabolism and blood flow in adults during cardiopulmonary bypass. *J Thorac Cardiovasc Surg* 1992; 103: 549–554.
  78. Hanks JH and Wallace RE. Relation of oxygen and temperature in the preservation of tissues by refrigeration. *Proc Soc Exp Biol Med* 1949; 71: 196–200.
  79. Jones PF and Siegel S. Temperature effects on the phosphorescence of aromatic hydrocarbons in poly(methylmethacrylate). *J Chem Phys* 1969; 50: 1134–1140.
  80. Pray HA, Schweickert CE and Minnich BH. Solubility of hydrogen, oxygen, nitrogen, and helium in water at elevated temperatures. *Ind Eng Chem* 1952; 44: 1146–1151.
  81. Rosomoff HL and Holaday DA. Cerebral blood flow and cerebral oxygen consumption during hypothermia. *Am J Physiol-Leg Content* 1954; 179: 85–88.
  82. Rossing RG and Cain SM. A nomogram relating pO<sub>2</sub>, pH, temperature, and hemoglobin saturation in the dog. *J Appl Physiol* 1966; 21: 195–201.
  83. Shirey MJ, Smith JB, Kudlik DE, et al. Brief anesthesia, but not voluntary locomotion, significantly alters cortical temperature. *J Neurophysiol* 2015; 114: 309–322.
  84. Soukup J, Zauner A, Doppenberg EMR, et al. The importance of brain temperature in patients after severe head injury: relationship to intracranial pressure, cerebral perfusion pressure, cerebral blood flow, and outcome. *J Neurotrauma* 2002; 19: 559–571.
  85. Sakadzic S, Yaseen MA, Jaswal R, et al. Two-photon microscopy measurement of cerebral metabolic rate of oxygen using periarteriolar oxygen concentration gradients. *Neurophotonics* 2016; 3: 045005.